

Spectrally indistinguishable intermodal-vectorial four-wave-mixing in birefringent few-mode fibers for spatial-polarization-frequency hybrid-entangled photon-pairs generation

ANDRZEJ GAWLIK,* MARTA BERNAŚ, KINGA ŻOŁNACZ, AND KAROL TARNOWSKI

Department of Optics and Photonics, Faculty of Fundamental Problems of Technology, Wrocław University of Science and Technology, 50-370 Wrocław, Poland

*andrzej.gawlik@pwr.edu.pl

Abstract:

In this paper, we investigate both experimentally and theoretically the two intermodal-vectorial four-wave-mixing processes in birefringent few-mode fibers, which are spectrally indistinguishable. We show that two four-wave-mixing processes involving the four polarization modes of different spatial distributions can overlap spectrally as long as the group refractive indices of the signal and idler modes intersect at the pump wavelength. The experimental confirmation of theoretical predictions is performed with PANDA fiber pumped with an Nd:YAG laser with 1064.3 nm wavelength. The spectral overlap enables the hybrid-entanglement of photons in spatial-polarization-frequency degrees of freedom. Moreover, we discuss that the spectral position of the overlapping FWMs can be tailored by: (i) the relative phase birefringence of the four modes participating in the FWM or (ii) the average chromatic dispersion of the signal/idler modes, allowing to move the process away from detrimental Raman scattering. Interestingly, in the ± 100 THz range from pump considered here, the gain of FWM depends primarily on the integral overlap between the modes participating in the process and is virtually wavelength-independent. This characteristic makes few-mode birefringent fibers a promising platform for developing flat-gain, spectrally tailored sources of photon pairs entangled in multiple degrees of freedom.

1. Introduction

The generation of entangled photon pairs plays a pivotal role in advancing modern quantum technologies, including quantum information processing and communication^{1,2}, quantum computing³, and quantum cryptography^{4,5}. Due to their compatibility with the existing communication networks, optical fibers represent a promising platform for the generation of entangled photon pairs through a nonlinear optical process of four-wave-mixing (FWM). In FWM, the annihilation of two pump photons leads to the simultaneous creation of two (signal and idler) photons, which are entangled in the energy-time domain⁶. Furthermore, the signal and idler photons can exhibit additional quantum relationships, such as (i) correlations, (ii) hyper-entanglement, or (iii) hybrid entanglement, in one or more degrees of freedom (DOFs), including polarization, spatial

distribution, or angular momentum⁷. The nature of these quantum relationships and the participating DOFs are determined by the dispersion characteristics of the considered fiber and the specific type of FWM process involved in the generation of the signal and idler photons. In essence, correlations are a natural consequence of the phase-matching during FWM (e.g., the signal/idler are generated in specific polarizations or transverse modes), while entanglement can be achieved through quantum interference^{8,9} of correlated photons or by spectrally overlapping distinct FWM processes^{10,11}. Importantly, generating entanglement across multiple DOFs can increase the capacity of quantum communication and improve transmission across noisy channels.

The last decade has marked a tremendous progress in generating photon pairs that are either correlated or entangled across multiple DOFs using FWM. Different fiber designs have facilitated the theoretical predication and experimental demonstration of schemes utilizing various FWM processes to achieve such correlations and entanglement. In single mode fibers (SMFs), the intramodal vectorial FWM was used to demonstrate entanglement in frequency⁸, polarization⁹, as well as hyperentanglement in energy/time-frequency and energy/time-polarization¹². As compared to SMFs, few-mode fibers (FMFs) offer the ability to excite higher-order mode thus extending the correlation/entanglement dimensionality by the spatial mode (also called transverse mode) degree of freedom. As a result, different research groups used intermodal or intermodal-vectorial FWM in FMFs to demonstrate: spatial correlations^{13,14} and entanglement¹⁵, spatial-frequency correlations^{10,16} and a scheme for such hybrid-entanglement^{10,11}. In our last work¹⁷, we used intermodal vectorial FWM to demonstrate the spatial-polarization-frequency correlations in a birefringent FMF.

In this manuscript, we use birefringent PANDA fiber (Fig. 1(a)) to experimentally demonstrate the generation of two spectrally overlapping intermodal-vectorial FWM, which can be used as a source of photon pairs with hybrid-entanglement in spatial-polarization-frequency degrees of freedom. This paper is organized in the following manner. In Section 2, we use the phase-matching of FWM to derive the conditions for the existence of spectrally overlapping intermodal-vectorial FWMs and show how the positions of the processes can be tuned spectrally to avoid overlap with the Raman band. In Section 3 we explain why that gain of FWM is mainly dependent on the overlap between the participating fields and not the spectral positions of the signal/idler. Finally, Section 4 contains the experimental demonstration of two spectrally overlapping intermodal-vectorial FWMs generated in a four-mode process. Interestingly, there exists another intermodal-vectorial FWM two-mode process which is correlated in spatial-polarization-frequency DOFs. The experimental observations are corroborated with numerical simulations confirming the spatial and polarization nature of participating modes.

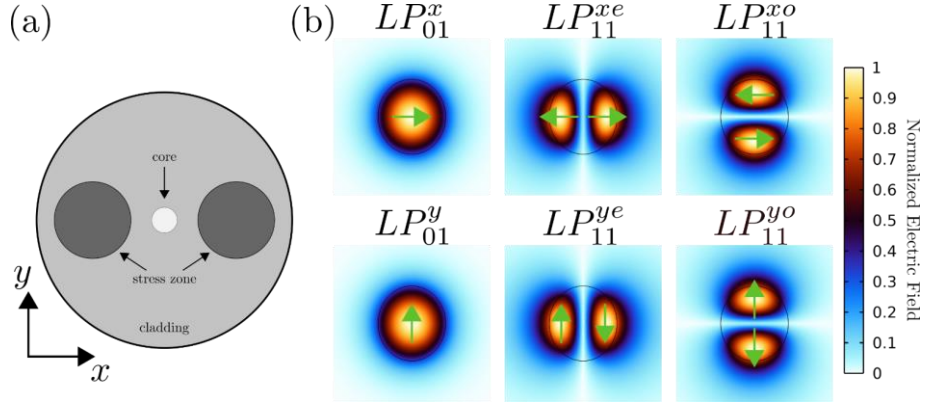


Fig. 1. (a) Schematic cross-section of the birefringent Nufern PM1550B-XP fiber with stress-applying zones. (b) The absolute values of the normalized electric fields of the six guided LP modes supported by the fiber at 1064.3 nm. The green arrows indicate the direction of the electric field, i.e., the polarization of the modes.

2. Phase-matching conditions

The observation of FWM requires the phase-matching of four electromagnetic waves participating in the process, which is mathematically expressed through their wavevectors as¹⁸ $\beta^{(l)} + \beta^{(m)} = \beta^{(p)} + \beta^{(n)}$, where superscripts l and m refer to the pumps waves, while p and n to, respectively, the signal and idler waves. The phase-matching condition for frequency-degenerate pumps can be approximated by a second-order Taylor series expansion at the pump frequency as:

$$\frac{\beta_2^{(p)} + \beta_2^{(n)}}{2} \Omega^2 + (\beta_1^{(p)} - \beta_1^{(n)}) \Omega + (\beta_0^{(p)} - \beta_0^{(l)} - \beta_0^{(m)} + \beta_0^{(n)}) = 0, \quad (1)$$

where $\beta_i^{(j)}$ describes the i^{th} derivative of the $j^{\text{th}} \in \{p, l, m, n\}$ mode wavevector and the angular frequency Ω (resp. $-\Omega$) describes the spectral detuning of the signal (resp. idler) from the pumps. Next, to build more intuition on how the linear optical properties of the fiber impact the phase-matching, we rewrite Eq.1 in the following manner:

$$-\frac{\lambda^2}{2\pi c} \underbrace{\left(\frac{D^{(p)} + D^{(n)}}{2}\right)}_{\bar{D}^{(p,n)}} \Omega^2 + \frac{1}{c} \underbrace{(N^{(p)} - N^{(n)})}_{\Delta N^{(p,n)}} \Omega + \underbrace{\left[\frac{(n^{(p)} - n^{(l)})}{\Delta n^{(p,l)}} - \frac{(n^{(m)} - n^{(n)})}{\Delta n^{(m,n)}}\right]}_{\Delta n} = 0, \quad (2)$$

where c is the speed of light, $D^{(p)}$ and $D^{(n)}$ (resp. $N^{(p)}$ and $N^{(n)}$) are the chromatic dispersion (resp. effective group refractive index) of the signal and idler modes, respectively, while $n^{(p)}, n^{(l)}, n^{(m)}, n^{(n)}$ are the effective refractive indices of the pump₁, pump₂, signal, and idler modes, respectively. Further, $\bar{D}^{(p,n)}$ and $\Delta N^{(p,n)}$ are, respectively, the average chromatic dispersion and the modal group birefringence of the signal/idler modes, while $\Delta n = \Delta n^{(p,l)} - \Delta n^{(m,n)}$ is the relative phase birefringence of the signal/pump₁ and idler/pump₂ modes. This allows to cast the phase-matching in a compact form, which highlights its quadratic nature:

$$-\frac{\lambda^2}{2\pi c} \bar{D}^{(p,n)} \Omega^2 + \frac{1}{c} \Delta N^{(p,n)} \Omega + \Delta n = 0. \quad (3)$$

The phase-matching given with Eq. 3 can lead to four different outcomes, depending on the number of modes involved and the relations between their optical parameters, as shown in Fig. 2. For a two-mode process (Fig. 2 (a)), $p = l$ and $m = n$, hence the free term of Eq. 3 is zero and we get one non-zero solution $\Omega = -\frac{2\pi}{\lambda^2} \frac{\Delta N^{(p,n)}}{\bar{D}^{(p,n)}}$. Further, when four modes participate in the FWM, three possible outcomes can take place. Namely: (i) there can be no phase-matching (Fig. 2 (b)), two solutions Ω_1, Ω_2 can appear either on (ii) the same (Fig. 2 (c)) or (iii) the opposite (Fig. 2 (d)) energy side from the pumps, which are both located at $\Delta\Omega = 0$. For the last scenario, we introduce a spectral distinguishability parameter $\delta\Omega = ||\Omega_1| - |\Omega_2||$, which describes the frequency difference between the signal (solid line) and idler (dashed line) bands localized on the same energy side from the pumps. Importantly, $\delta\Omega$ describes the frequency difference between two modes (p and n) of different polarizations and/or orders.

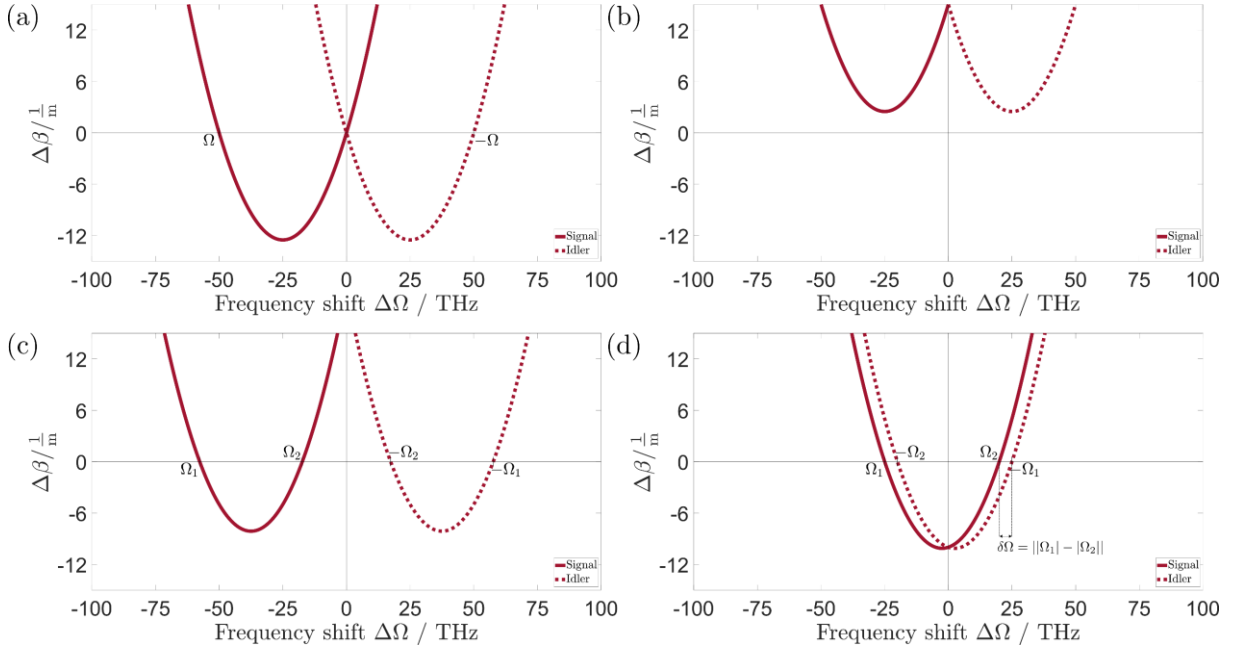


Fig. 2. Phase-matching condition of FWM calculated for four distinct cases: (a) two-mode process, (b) four-mode process, where there is no phase-matching, (c) four-mode process, where both solutions Ω_1, Ω_2 appear at the same energy side of the pumps, and (d) four-mode process, where Ω_1, Ω_2 appear at the opposite energy sides of the pumps. Solid (resp. dashed) lines represent the signal (Ω) (resp. idler ($-\Omega$)) solution.

From the quadratic nature of Eq. 3, it is straightforward that $\delta\Omega \rightarrow 0$ when $\Delta N^{(p,n)} \rightarrow 0$. This is confirmed in Fig. 3 (a), which shows that if one reduces $\Delta N^{(p,n)}$ the signal (solid lines) and idler bands (dashed lines) converge to one another. Setting $\Delta N^{(p,n)} = 0$ (green lines) leads to the appearance of two pairs of overlapping solutions located at $\Delta\Omega = \pm|\Omega_1| = \pm|\Omega_2|$. From the physical perspective, equalizing the group refractive indices of the signal and idler modes results in the generation of two pairs of overlapping peaks in the spectrum. The photons created in the two peaks located at $\Delta\Omega = +|\Omega_1|$ are spectrally

indistinguishable ($\delta\Omega = 0$) and, via FWM, exhibit spatial-polarization correlation with the photons created at $\Delta\Omega = -|\Omega_1|$. This allows for the generation of two-photon states with hyper-entanglement in spatial-polarization-frequency DOFs through intermodal-vectorial FWM, under the requirement that $\Delta N^{(p,n)} \rightarrow 0$ at the pump wavelength.

Subsequently, the spectral position of the spectrally indistinguishable peaks can be tailored by keeping $\Delta N^{(p,n)} = 0$ and varying either the free term (Δn) or the quadratic term ($\bar{D}^{(p,n)}$) of Eq. 3, as shown in, respectively, Figs. 3 (b) and (c).

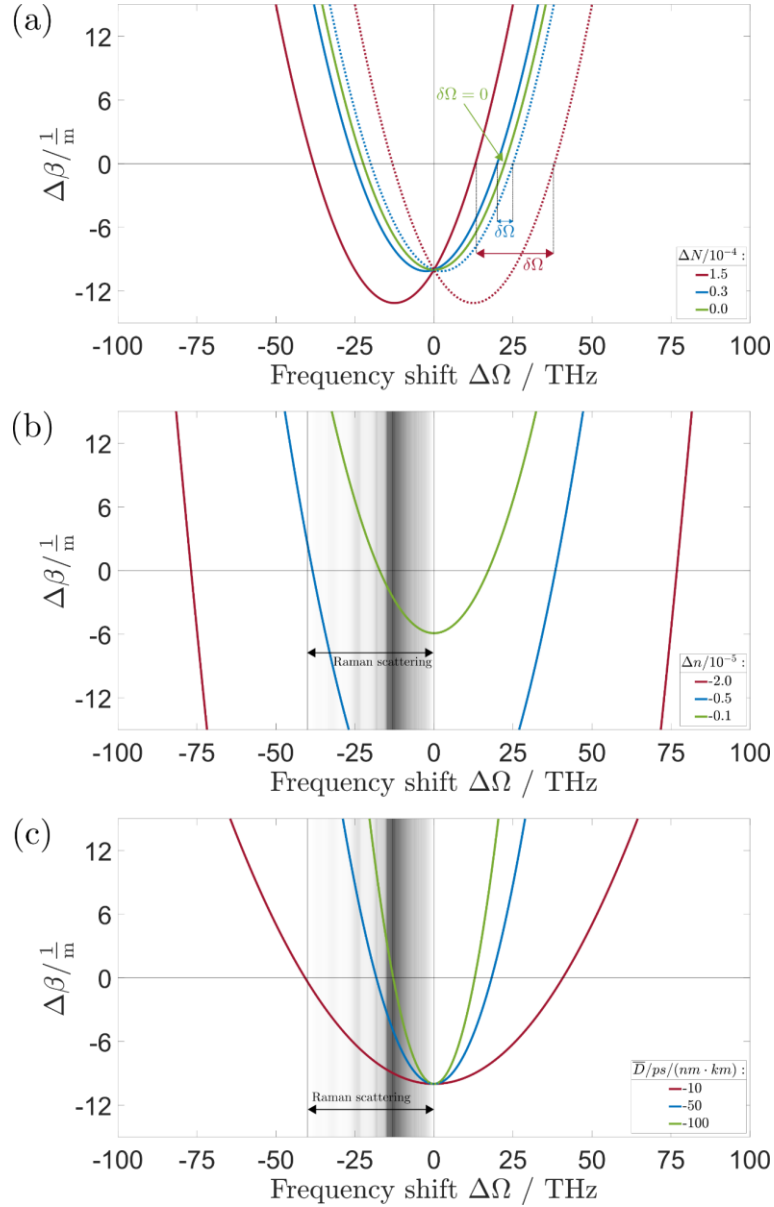


Fig. 3. Impact of the (a) modal group birefringence of the signal/idler modes ΔN , (b) relative phase birefringence of the signal/pump₁ and idler/pump₂ modes Δn , and (c) average chromatic dispersion of the signal/idler modes \bar{D} on the spectral positions of the signal/idler bands generated in a four-mode intermodal-vectorial FWM. Solid (resp. dashed) lines represent the signal (Ω) (resp. idler ($-\Omega$)) solution. $\delta\Omega$ is the spectral distinguishability parameter. The inverted grayscale intensity map, where white (resp. black) corresponds to 0 (resp. 1) in (b) and (c) shows the normalized intensity of the Raman scattering, which is significant for signals redshifted from 0 to 40 THz from the pump frequency.

However, from a practical point of view, it is easier to vary the relative phase birefringence between the modes (Δn) rather than the average chromatic dispersion ($\bar{D}^{(p,n)}$), without significantly affecting $\Delta N^{(p,n)}$. For example, Δn can be changed by tailoring the core ellipticity or shape and size of stress zones inside the fiber (e.g., PANDA, Bow-Tie). In the first approximation, such zones shift the stress-free effective phase refractive indices of the modes by a dispersionless constant, thus having a minimal impact on the effective group indices and $\Delta N^{(p,n)}$. Finally, the ability to manipulate the spectral position of such FWM is important in: (i) tailoring the process for a particular application and (ii), in terms of entanglement, moving the FWM away from the region of significant Raman scattering (0-40 THz redshift from the pump¹⁸), which acts as a noise mechanisms deteriorating the signal-idler correlations^{7,19}. The normalized intensity of the Raman scattering is superimposed in Figs. 3 (b) and (c) as an inverted grayscale intensity map, where white (resp. black) corresponds to 0 (resp. 1).

3. Gain of FWM

Phase-matching between a set of fiber modes is a necessary condition for FWM to occur, but it alone is not sufficient. Apart from it, the modes require a non-zero integral overlap between their respective electromagnetic fields. This overlap defines the strength of the FWM process and is given by²⁰:

$$S_K^{plmn} = \frac{2}{3} \left| \frac{\langle [\mathbf{F}_p^* \mathbf{F}_l] [\mathbf{F}_m \mathbf{F}_n^*] \rangle}{[\langle |\mathbf{F}_p|^2 \rangle \langle |\mathbf{F}_l|^2 \rangle \langle |\mathbf{F}_m|^2 \rangle \langle |\mathbf{F}_n|^2 \rangle]^{1/2}} \right| + \frac{1}{3} \left| \frac{\langle [\mathbf{F}_p^* \mathbf{F}_n] [\mathbf{F}_m \mathbf{F}_l] \rangle}{[\langle |\mathbf{F}_p|^2 \rangle \langle |\mathbf{F}_l|^2 \rangle \langle |\mathbf{F}_m|^2 \rangle \langle |\mathbf{F}_n|^2 \rangle]^{1/2}} \right|, \quad (5)$$

where $\mathbf{F}_j(x, y)$ represents the spatial distribution of the $j^{th} \in \{p, l, m, n\}$ fiber mode (see Fig. 1 (b)) while the integration in the brackets is carried out over the x and y coordinates. To describe the relative strength of different FWM processes, it is convenient to normalize S_K^{plmn} with respect to the self-overlap of the fundamental mode S_K^{xxxx} , i.e., $f^{plmn} = S_K^{plmn} / S_K^{xxxx}$.

Table 1 summarizes f^{plmn} of some representative FWM processes which can take place in the fiber shown in Fig. 1 (a) when phase-matched. The overlaps were calculated at 1064.3 nm using COMSOL²¹. At this wavelength, the fiber supports 6 polarization modes divided into two spatial LP_{01} and LP_{11} groups (see Fig. 1 (b)). As shown, the fiber supports: vectorial (V), intermodal (I), as well as 2-mode and 4-mode intermodal-vectorial (IV) processes, with the last one being of particular interest in here due to its possible spectral indistinguishability. For a thorough discussion of the relative strength of different FWM processes in the PANDA fiber we refer to¹⁷.

Table 1. Integral overlap $f^{plmn} = S_K^{plmn} / S_K^{xxxx}$ of selected FWM processes with excitable in the fiber from Fig. 1.

	<i>signal</i>	<i>pump₁</i>	<i>pump₂</i>	<i>idler</i>	
process type	p	l	m	n	f^{plmn}
<i>V</i>	LP_{01}^x	LP_{01}^x	LP_{01}^y	LP_{01}^y	0.667
<i>I</i>	LP_{01}^y	LP_{01}^y	LP_{11}^{ye}	LP_{11}^{ye}	0.530
<i>V</i>	LP_{11}^{yo}	LP_{11}^{yo}	LP_{11}^{xo}	LP_{11}^{xo}	0.529
<i>IV (2 modes)</i>	LP_{01}^y	LP_{01}^y	LP_{11}^{xe}	LP_{11}^{xe}	0.353
<i>IV (2 modes)</i>	LP_{11}^{xo}	LP_{11}^{xo}	LP_{11}^{ye}	LP_{11}^{ye}	0.170
<i>IV (4 modes)</i>	LP_{11}^{ye}	LP_{01}^y	LP_{11}^{xe}	LP_{01}^x	0.353
<i>IV (4 modes)</i>	LP_{11}^{ye}	LP_{11}^{yo}	LP_{11}^{xe}	LP_{11}^{xo}	0.167

Next, we establish the relationship between the strength of the FWM process (S_K^{plmn}) and its gain. To derive the gain, we neglect Raman scattering and assume that: (i) the pump powers are significantly higher than those of the signal and idler bands, and (ii) the pumps remain undepleted during the FWM generation. Under these assumptions, it can be shown that the gain of the FWM is given by:

$$g = \frac{-i\kappa + 4\sqrt{\left(\frac{n_2}{c}\right)^2 \omega_p \omega_n (S_K^{plmn})^2 P_1 P_2 - \left(\frac{\kappa}{4}\right)^2}}{2}, \quad (6)$$

where n_2 is the nonlinear refractive index, ω_p (resp. ω_n) is the signal (resp. idler) angular frequency, P_l are P_m are the pump powers, and κ is the power-dependent effective phase-mismatch¹⁸.

The maximum gain is achieved for $\kappa = 0$:

$$g_{max} = \frac{2n_2}{c} \underbrace{\sqrt{\omega_p \omega_n}}_{\bar{\omega}} \underbrace{\sqrt{P_l P_m}}_{\bar{P}} S_K^{plmn}, \quad (7)$$

where $\bar{\omega}$ and \bar{P} represent the power geometric means of the signal/idler frequencies and the pump powers, respectively.

Let us now discuss how $\bar{\omega}$, \bar{P} , and S_K^{plmn} impact maximum gain of FWM. Starting with \bar{P} and assuming a constant total pump power $P_0 = P_l + P_m$, it is straightforward that g_{max} increases from 0 for $P_{l(m)} = 0$ in a square root fashion reaching its maximum when $P_l = P_m$. Second, assuming the pumps of equal frequency ($\omega_l = \omega_m$), $\bar{\omega}$ is maximal for $\omega_p = \omega_n = \omega_l = \omega_m$ and decreases for increasing detuning from the pumps. However, $\bar{\omega}$ has a negligible impact on g_{max} in the considered ± 100 THz range from the pumps centered at 1064.3 nm. Indeed, in our case, even for the signal/idler bands detuned by 100 THz, $\bar{\omega}$ drops only by around 6 % as compared to its maximum value. Third, g_{max} is a linear function of S_K^{plmn} and, in our case, can vary up to four times depending on the on

the modes participating in the FWM (see Table 1, $(LP_{11}^{yo}, LP_{11}^{xe}) \rightarrow (LP_{11}^{ye}, LP_{11}^{xo})$ vs. $(LP_{01}^x, LP_{01}^y) \rightarrow (LP_{01}^x, LP_{01}^y)$). Finally, we want to emphasize that under even pump excitation ($P_l = P_m$) the gain of FWM is primarily dependent on S_K^{plmn} hence the modes selected for the process and not the frequency detuning of the signal/idler bands from the pump. Interestingly, it allows for tailoring of the spectral position of a specific intermodal-vectorial FWM (see Figs. 3 (b) and (c)) while keeping the gain virtually constant vs. the wavelength.

4. Experimental verification

Subsequently, we use the PANDA fiber shown in Fig. 1 to experimentally demonstrate spectrally indistinguishable intermodal-vectorial FWM involving four modes leading to the generation of two spectrally overlapping pairs of peaks. The spectra shown in Fig. 4 (a) were measured using the Nd:YAG pump laser centered at 1064.3 nm with 19 kHz repetition rate, pulse duration of 1 ns, and an average power of 140 mW. To generate the relevant FWM process, the pump laser was split into LP_{01}^y and LP_{11}^{xe} modes using the Wollaston prism²². Adding a polarizer at the output of the fiber allowed to resolve the unpolarized spectrum (blue line) into the x - (orange line) and y -polarized (yellow line) components, which revealed the spectral overlap between two pairs of peaks located around 1021.5 and 1111 nm.

To identify the origin of these overlapping peaks, Fig. 4 (b) displays the mode-resolved spectra generated numerically by solving the Generalized Multimode Nonlinear Schrodinger equation (GMMNLSE)²³ using the implementation provided by Chen et. al²⁴. As can be seen, each pair of the overlapping peaks is related to the LP_{01}^x and LP_{11}^{ye} modes thus corresponds to the $(LP_{01}^y, LP_{11}^{xe}) \rightarrow (LP_{01}^x, LP_{11}^{ye})$ intermodal-vectorial FWM process involving four modes. The spectral positions of the experimental and numerical peaks are in good agreement, while the numerical peaks are narrower which is expected due to imperfections in real fibers. For the numerical calculations we used the linear optical properties of the fiber measured experimentally (Fig. 5) and assumed a continuous wave excitation source of 1000 W evenly distributed into the LP_{01}^y and LP_{11}^{xe} modes. The reason why the spectral distinguishability parameter $\delta\Omega$ is non-zero in both experimental and numerical spectra is linked to the fact that the crossing of N_{eff} of the LP_{01}^x and LP_{11}^{ye} modes (Fig. 5 (b)) takes place at wavelength slightly shorter than the pump wavelength. However, the substantial spectral overlap between the peaks opens the possibility to generate hybrid-entangled photon pairs in spatial-polarization-frequency DOFs in the considered fiber.

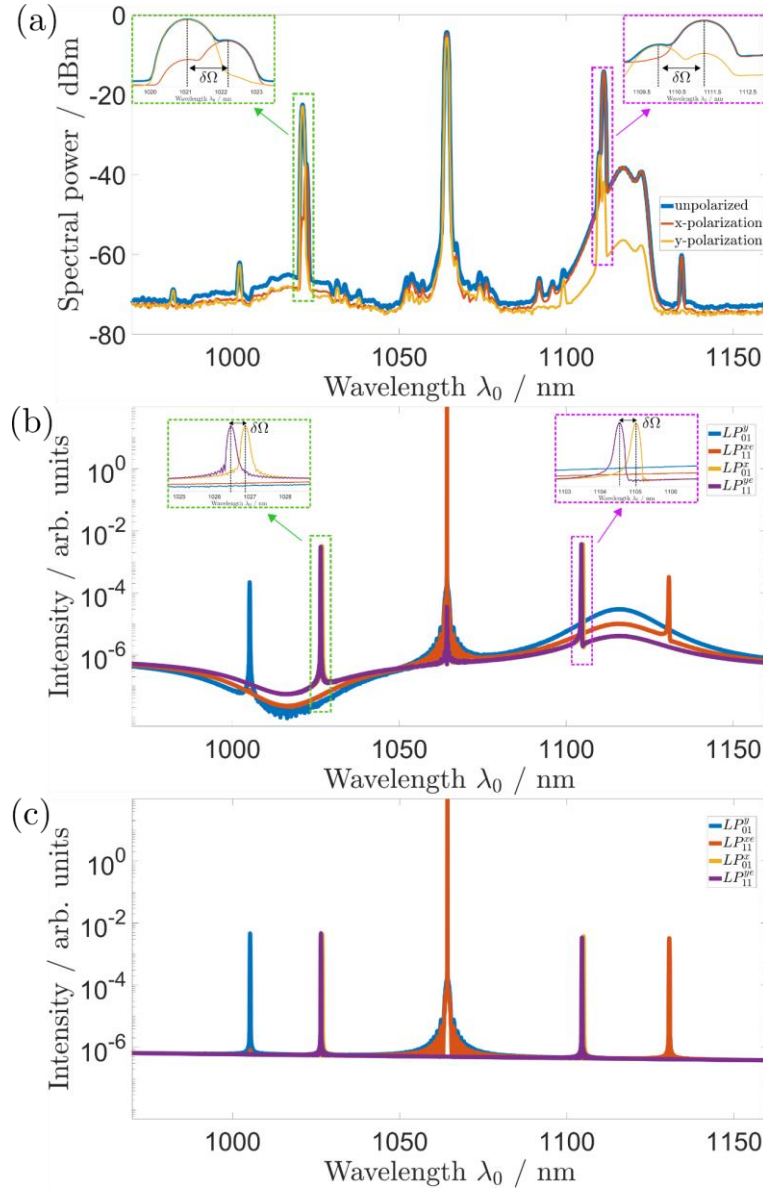


Fig. 4. (a) Polarization-resolved experimental spectra. (b, c) Mode-resolved numerically spectra generated with the Generalized Multimode Nonlinear Schrodinger equation (GMMNLSE). In (b) (resp. (c)) we included (resp. excluded) the Raman term in the GMMNLSE. For all the spectra the excitation of the LP_{01}^y and LP_{11}^{xe} modes from Fig. 1 (b) was used. The insets in (a) and (b) show the zoom-in on the spectrally overlapping peaks of spectrally indistinguishable FWM.

Interestingly, there are two additional peaks at 1002 and 1134 nm that appear in the experimental spectra. As confirmed with the numerical results, they are generated in two-mode intermodal-vectorial FWM (LP_{01}^y, LP_{11}^{xe}) \rightarrow (LP_{01}^y, LP_{11}^{xe}), which is correlated in spatial-polarization-frequency DOFs. Interestingly, according to Table 1 and Eq. 7, the gains (hence the peak heights) of four-mode (LP_{01}^y, LP_{11}^{xe}) \rightarrow (LP_{01}^x, LP_{11}^{ye}) and two-mode (LP_{01}^y, LP_{11}^{xe}) \rightarrow (LP_{01}^y, LP_{11}^{xe}) FWM processes should be almost identical, with small difference related to $\bar{\omega}$. However, as can be seen in both the experimental and numerical spectra, this is not the case as the peaks related to the two-mode intermodal-vectorial FWM are significantly lower than the ones generated in the four-mode process. This discrepancy is linked to the Raman scattering, which reduces the gain of FWM by

competing with it¹⁸. This is confirmed with Fig. 4 (c), which shows that by neglecting the Raman term in the GMMNLSE the peak heights hence gains of the processes are equal.

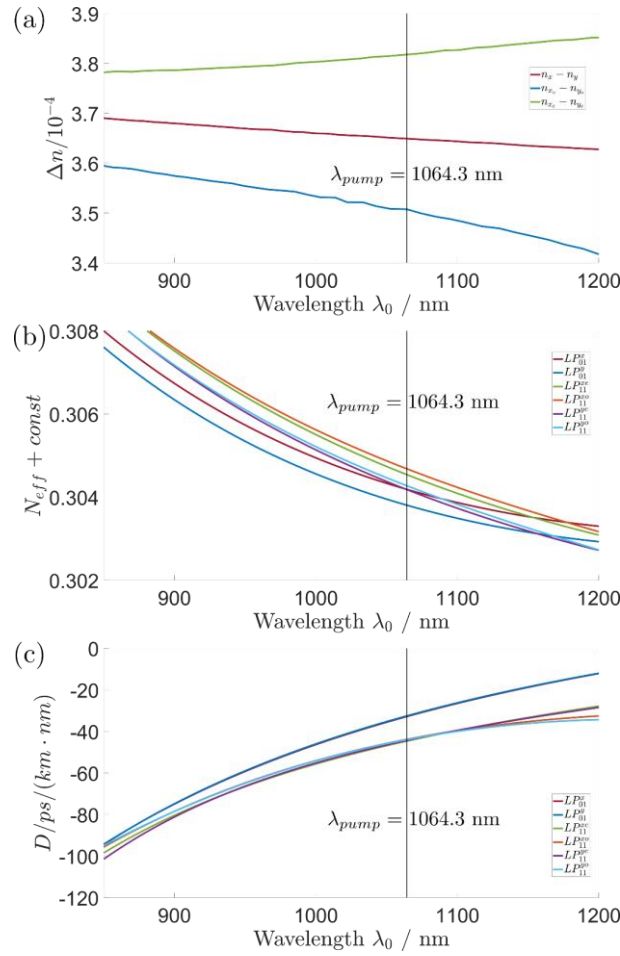


Fig. 5. Optical parameters of the fiber PM1550B-XP measured using spectral interference method^{25,26}. (a) The difference in the phase refractive indices between the modes of the same spatial distribution and different polarization (x and y). (b) The group refractive indices of the modes obtained with precision to a constant. (c) The chromatic dispersion D of the modes calculated from (b).

Importantly, the spectral overlap of the two discussed four-mode intermodal-vectorial FWMs opens up a possibility of generating photon pairs entangled in multiple DOFs. For example, by spectrally selecting these processes and using appropriate filtering one can build a quantum state with the spatial-polarization hybrid-entangled in a form of $|\psi\rangle = \frac{1}{\sqrt{2}}(|x\rangle|m_1\rangle + e^{-i\phi}|y\rangle|m_2\rangle)$, where H and V (resp. m_1 and m_2) are the polarizations (resp. the spatial distributions) of the signal and idler modes, and ϕ is the relative phase between the signal and idler photons. Such states can be used to experimentally study the violation of the classical limits given by the Bells inequality²⁷.

Before concluding, it is important to emphasize that, while we studied FWM in the same commercially available fiber, we observed different processes and peak positions compared to the previous study¹⁷. This discrepancy is due to variations in the propagation

parameters of the two PANDA fibers from different lots. This highlights the importance of robust design of fibers for nonlinear optical conversion processes like FWM.

5. Conclusions

To conclude we demonstrated experimentally and explained theoretically the generation of spectrally indistinguishable intermodal-vectorial four-wave-mixing in a few-mode birefringent fiber. We showed that spectrally overlapping FWMs can be achieved in a four-mode process once the group refractive indices of the signal and idler intersect at the pump wavelength. Further, we discussed how the processes can be spectrally tailored to mitigate the detrimental Raman scattering by changing either the relative phase birefringence Δn of the four modes participating in the FWM or the average chromatic dispersion of the signal/idler $\bar{D}^{(p,n)}$. Interestingly, such spectral tailoring has a negligible impact on the gain as long as the signal/idler are not far-detuned from the pumps²⁸. Finally, this work shows that spectrally indistinguishable intermodal-vectorial four-wave-mixing generated in a few-mode birefringent fiber is a promising candidate as a source of photon pairs with hybrid-entanglement in the spatial-polarization-frequency degrees of freedom.

Funding

Narodowe Centrum Nauki (2018/30/E/ST7/00862).

Bibliography

1. Mattle, K., Weinfurter, H., Kwiat, P. G. & Zeilinger, A. Dense Coding in Experimental Quantum Communication. *Phys Rev Lett* **76**, (1996).
2. Zoller, P. *et al.* Quantum information processing and communication: Strategic report on current status, visions and goals for research in Europe. *European Physical Journal D* **36**, (2005).
3. Kwiat, P. G. *et al.* New High-Intensity Source of Polarization-Entangled Photon Pairs. *Phys Rev Lett* **75**, (1995).
4. Gisin, N., Goire Ribordy, G., Tittel, W. & Zbinden, H. Quantum cryptography. *Rev Mod Phys* **74**, (2002).
5. Jennewein, T., Simon, C., Weihs, G., Weinfurter, H. & Zeilinger, A. Quantum Cryptography with Entangled Photons. *Phys Rev Lett* **84**, (2000).
6. Dong, S. *et al.* Energy-time entanglement generation in optical fibers under CW pumping. *Opt Express* **22**, (2014).
7. Garay-Palmett, K. *et al.* Fiber-based photon-pair generation: tutorial. *Journal of the Optical Society of America B* **40**, (2023).
8. Zhou, Q., Zhang, W., Yuan, C., Huang, Y. & Peng, J. Generation of 1.5 μm discrete frequency-entangled two-photon state in polarization-maintaining fibers. *Opt Lett* **39**, (2014).
9. Zhu, F., Zhang, W. & Huang, Y. Fiber-based frequency-degenerate polarization entangled photon pair sources for information encoding. *Opt Express* **24**, (2016).

10. Cruz-Delgado, D. *et al.* Fiber-based photon-pair source capable of hybrid entanglement in frequency and transverse mode, controllably scalable to higher dimensions. *Sci Rep* **6**, (2016).
11. Ekici, Ç. & Dinleyici, M. S. Graded-index optical fiber transverse-spatial-mode entanglement. *Phys Rev A* **102**, (2020).
12. Dong, S. *et al.* Generation of hyper-entanglement in polarization/energy-time and discrete-frequency/energy-time in optical fibers. *Sci Rep* **5**, (2015).
13. Guo, C., Su, J., Zhang, Z., Cui, L. & Li, X. Generation of telecom-band correlated photon pairs in different spatial modes using few-mode fibers. *Opt Lett* **44**, (2019).
14. Sulimany, K. & Bromberg, Y. All-fiber source and sorter for multimode correlated photons. *npj Quantum Inf* **8**, (2022).
15. Shamshooli, A., Guo, C., Parmigiani, F., Li, X. & Vasilyev, M. Progress Toward Spatially-Entangled Photon-Pair Generation in a Few-Mode Fiber. *IEEE Photonics Technology Letters* **33**, (2021).
16. Garay-Palmett, K. *et al.* Photon-pair generation by intermodal spontaneous four-wave mixing in birefringent, weakly guiding optical fibers. *Phys Rev A* **93**, (2016).
17. Majchrowska, S., Żońnac, K., Urbańczyk, W. & Tarnowski, K. Multiple intermodal-vectorial four-wave mixing bands generated by selective excitation of orthogonally polarized LP 01 and LP 11 modes in a birefringent fiber. *Opt Lett* **47**, (2022).
18. Agrawal, G. P. *Nonlinear Fiber Optics*. (Elsevier, 2019).
19. Rottwitt, K., Koefoed, J. G. & Christensen, E. N. Photon-pair sources based on intermodal four-wave mixing in few-mode fibers. *Fibers* **6**, (2018).
20. Horak, P. & Poletti, F. Multimode Nonlinear Fibre Optics: Theory and Applications. in *Recent Progress in Optical Fiber Research* (2012).
21. COMSOL Multiphysics®, www.comsol.com (2024).
22. Żońnac, K. & Urbanczyk, W. Selective excitation of different combinations of LP 01 and LP 11 polarization modes in a birefringent optical fiber using a Wollaston prism. *Opt Express* **30**, (2022).
23. Wright, L. G. *et al.* Multimode nonlinear fiber optics: Massively parallel numerical solver, tutorial, and outlook. *IEEE Journal of Selected Topics in Quantum Electronics* **24**, (2018).
24. Chen, Y.-H., Haig, H., Wu, Y., Ziegler, Z. & Wise, F. Accurate modeling of ultrafast nonlinear pulse propagation in multimode gain fiber. *Journal of the Optical Society of America B* **40**, (2023).
25. Kowal, D. *et al.* Measurement of birefringence and ellipticity of polarization eigenmodes in spun highly birefringent fibers using spectral interferometry and lateral point-force method. *Opt Express* **26**, (2018).
26. Żońnac, K., Szatkowski, M., Masajada, J. & Urbanczyk, W. Broadband chromatic dispersion measurements in higher-order modes selectively excited in optical fibers using a spatial light modulator. *Opt Express* **29**, (2021).
27. Barreiro, J. T., Langford, N. K., Peters, N. A. & Kwiat, P. G. Generation of hyperentangled photon pairs. *Phys Rev Lett* **95**, (2005).
28. Stefańska, K. *et al.* High-gain far-detuned nonlinear frequency conversion in a few-mode graded-index optical fiber. *Sci Rep* **14**, (2024).